Cav03-OS-7-019

Fifth International Symposium on Cavitation (CAV2003)
Osaka, Japan, November 1-4, 2003

FULLY COUPLED, 6-DOF TO URANS, MODELING OF CAVITATING FLOWS AROUND A SUPERCAVITATING VEHICLE

Jules W. Lindau **Robert F. Kunz**

Jason M. Mulherin **James J. Dreyer** **David R. Stinebring**

Applied Research Lab/The Pennsylvania State University

ABSTRACT

A preconditioned, homogenous, multiphase, unsteady Reynolds Averaged Navier-Stokes (URANS) scheme is dynamically coupled to a six-degree-of-freedom (6DOF) rigid body motion model. Details of the numerical and physical modeling associated with the coupled URANS-6DOF code are presented. Results are presented for an application to a notional supercavitating vehicle. Among other important observations, the vehicle dynamics solution is seen to approach a quasi-steady limit cycle behavior. This compares favorably with integrated results of a reduced order dynamics model.

INTRODUCTION

Cavitation in hydrodynamic applications usually has a negative impact, leading to excessive noise and damage to marine components. However, the potential reduction in drag associated with supercavitation has led to interest in supercavitating hydrofoils, fast ships, and high speed supercavitating vehicles [1]. The bodies of these vehicles are completely enshrouded in a gaseous cavity, that emanates downstream of a cavitator placed at the nose; only control surfaces remain in continuous contact with liquid. These include the cavitator, and may include control fins, or some other appendages [2]. The supercavity is generally composed of some water vapor mixed with noncondensable injected gas. To support the supercavity, the cavitator may be required to generate a certain amount of natural (vaporous) cavitation. The cavitator must initiate the cavity and remains wetted during operation. Downstream of the cavitator, ventilation gas may be used to enhance and stablilize the cavity. Natural cavitation occurs as liquid water flows around the cavitator due to a drop in pressure, and the supercavity is enhanced and sustained by ventilation gas. The gas within the cavity is separated, and at a near uniform pressure. A schematic drawing of a notional supercavitating vehicle is shown in Figure 1 (a). A close up of the computational model of this vehicle is shown in Figure 1 (b), and illustrates the flat, disk shaped cavitator and downstream ventilation ports.

The dynamics of a supercavitating vehicle are complex, requiring research level efforts specific to multiple disciplines of science and engineering. Even when reduced order physics are considered, as is the usual practice, obtaining tractable dynamics for the design of such a vehicle is a major task. Recently, workers have presented a model of supercavitating vehicle dynamics suitable for evaluation of control systems based on a reduced order fluid and vehicle dynamics model [3]. Other workers have applied more complex fluid dynamics models coupled to vehicle dynamics [2]. In general, elegant cavity dynamics models follow credible theory [4 and 5], but when applied to a complex physical situation, such as unsteady flow interacting with a rocket-propelled, maneuvering, supercavitating vehicle, further validation and tuning may be necessary. Specifically, although these models consider a great deal of the evident physics, they are inherently incapable of accommodating some potentially important flow physics including some or all of: viscous effects, vortical flows, compressibility and mass transfer. Nevertheless, reduced-order dynamics models remain valuable for supercavitating vehicle design, due to their ease of solution and analytic tractability. Such models, when carefully applied, may yield physical insight not easily obtained from more complex, computationally intensive models. Also, it is unlikely that any computational methods will ever replace the need for full-scale open-water testing of such a vehicle.

In the present work, the authors have pursued an unsteady Reynolds Averaged Navier-Stokes level of flow field modeling, with the intent of improving the accuracy of dynamics modeling used for design of supercavitating vehicles, and for validation of lower order dynamic modeling. The paper is organized as follows: The physical and algorithmic formulation of the modeling method is described. Coupled multiphase URANS-6DOF results are presented for a nominal supercavitating vehicle. Qualitative comparisons are made with a simpler dynamic model, and conclusions regarding the URANS-6DOF method are drawn.

NOMENCLATURE	
A	mass matrix
B	vehicle buoyancy
b	inertial coupling vector
C_1, C_2	turbulence model constants
C_q	dimensionless ventilation rate $[Q/(U_0 D_c^2)]$ (Q is volume flow rate)
C_ϕ	mass transfer model parameter
D_c	cavitator diameter
Fr	Froude Number $[U_O/(Lg)^{1/2}]$
F_x, F_y, F_z, M_x, M_y, M_z	hydrodynamic forces and moments on vehicle
f	vector of forces on vehicle
k, ε	turbulence model eddy viscosity and specific dissipation rate
L	vehicle length
m	vehicle mass
P	turbulence model production term
Pr_{tk}, $Pr_{t\varepsilon}$	turbulent Prandtl Numbers for k and ε
p, q, r	vehicle relative rotation rates (also p is thermodynamic pressure)
p_v	saturation vapor pressure
s	rigid-body motion dependent variable vector
t_∞	time parameter in mass transfer model
u_B, v_B, w_B, u, v, w	vehicle (relative) velocities and fluid (absolute) velocities
Q,Q_c	fluid dynamics primitive and conservative solution variable vectors
W	vehicle weight
x_G, y_G, z_G, x_B, y_B, z_B	coordinates of vehicle center of gravity and center of buoyancy (body reference frame)
y^+	dimensionless wall distance (boundary layer)
I_x, I_y, I_z, I_{xy}, I_{zx}, I_{yz}	vehicle relative moments and products of inertia
$\alpha_L, \alpha_{ng}, \alpha_v$	liquid, non-condensable, and vapor volume fractions
β	preconditioning parameter
Γ^p	preconditioning matrix
γ_g	specific gravity of vehicle
ϕ, θ, ψ	vehicle absolute Euler angles
$\mu_{m,t}$	mixture eddy viscosity
ρ_m, ρ_L, ρ_{ng}, ρ_v	mixture, liquid, non-condensable gas, and vapor densities
σ	cavitation index $[(p_\infty - p_v)/(0.5\rho_L U_o^2)]$
ξ, η, ζ	finite-volume structured coordinates

METHODOLOGY

The modeling method is as follows: A high-fidelity multiphase fluid dynamics model, suitable for turbulent, high Reynolds Number flows (multiphase URANS) is coupled to the general equations of vehicle/rigid body motion (6DOF). Thus the URANS and the 6DOF are submodels to be coupled for solution of the overall model problem. Coupling between the submodels is achieved via modeling the shear and normal forces on the surface of the rigid body. The shear and normal forces are results of the instantaneous solution to the URANS. In this model, the normal forces include both the pressure on solid surfaces and the impulse through propulsion and ventilation computational boundaries. Shear forces are computed based on a turbulent wall function. The URANS forces are then resolved into appropriate instantaneous force and moment components for the 6DOF. The result of the 6DOF solution is then translation and rotation of the rigid body. With adequate discretization, the 6DOF and the URANS then tend to the proper physics. The current presentation and results are for a single, completely rigid, body and closely follow the methodology of Dreyer [6] for single-phase flow. Formulation of the single-phase pseudocompressible formulation for nonstationary grid systems has been well presented by Taylor [7]. Solutions with multiple bodies, or a single body with articulated control surfaces, represent straightforward extensions of the current methodology.

6-DEGREE-OF-FREEDOM PHYSICAL MODELING

Computation of fully coupled multiphase URANS-6DOF modeling is achieved with a computational flow grid fixed to the rigid body. Flow solution is then obtained in an inertial reference frame. The rigid body motion problem is solved in a body-fixed reference frame. These choices follow the work of Dreyer et al. [6]. During each physical time step, the hydrodynamic forces on the body are computed based on the current flow field solution, then the position of the body, is updated based upon solution of the 6DOF equations, and then the flow solution is updated.

The 6DOF rigid body motion governing equation system may be expressed as Eq. 1:

$$A\frac{ds}{dt} = (f - b) \tag{1}$$

Here A is the mass matrix, s contains velocity and rotation rate, b is the inertial coupling, and f contains applied forces and moments. Forces considered in this effort are due to gravity, buoyancy, and fluid dynamics. The mass matrix for this reference frame is given in Eq. 2.

$$A = \begin{bmatrix} m & 0 & 0 & 0 & m z_G & -m y_G \\ 0 & m & 0 & -m z_G & 0 & m x_G \\ 0 & 0 & m & m y_G & -m x_G & 0 \\ 0 & -m z_G & m y_G & I_x & -I_{xy} & -I_{zx} \\ m z_G & 0 & -m x_G & -I_{xy} & I_y & -I_{yz} \\ -m y_G & m x_G & 0 & -I_{zx} & -I_{yz} & I_z \end{bmatrix} \tag{2}$$

Here, m is the actual mass of the vehicle, and x_G, y_G, z_G are the coordinates of the center of mass, I_x, I_y, I_z are the moments of inertia, and I_{xy}, I_{xz}, I_{yz} are the products of inertia, all in the body fixed reference frame. The rigid body motion solution quantities are the vehicle velocity and rotation rate vector and are contained in s, defined in Eq. 3:

$$s = (u_B, v_B, w_B, p, q, r)^T \tag{3}$$

u,v, and *w* are the body-fixed velocity components and *p,q,* and *r* are the body-fixed rotation rates. The inertial coupling vector arises from solution of the equations of motion in a noninertial frame and is given in Eq. 4:

$$b = \begin{bmatrix} m\left[w_B q - v_B r - x_G\left(q^2 + r^2\right) + y_G pq + z_G pr\right] \\ m\left[u_B r - w_B p - y_G\left(r^2 + p^2\right) + z_G qr + x_G qp\right] \\ m\left[v_B p - u_B q - z_G\left(p^2 + q^2\right) + x_G rp + y_G rq\right] \\ \left(I_z - I_y\right) qr - I_{xz} pq + I_{yz}\left(r^2 - q^2\right) + I_{xy} pr + m\left[y_G\left(v_B p - u_B q\right) - z_G\left(u_B r - w_B p\right)\right] \\ \left(I_z - I_z\right) rp - I_{xy} qr + I_{xz}\left(p^2 - r^2\right) + I_{zy} qp + m\left[z_G\left(w_B q - v_B r\right) - x_G\left(v_B p - u_B q\right)\right] \\ \left(I_y - I_x\right) pq - I_{yz} rp + I_{xy}\left(q^2 - p^2\right) + I_{zx} rq + m\left[x_G\left(u_B r - w_B p\right) - y_G\left(w_B q - v_B r\right)\right] \end{bmatrix} \tag{4}$$

Finally, the fluid dynamic forces are combined with the gravitational and buoyancy terms and written in vector form in Eq 5:

$$f = \begin{bmatrix} -(W - B)\sin\theta + F_x \\ (W - B)\cos\theta \sin\phi + F_y \\ (W - B)\cos\theta \cos\phi + F_z \\ \left(y_G W - y_B B\right)\cos\theta \cos\phi - \left(z_G W - z_B B\right)\cos\theta \sin\phi + M_x \\ -\left(x_G W - x_B B\right)\cos\theta \cos\phi - \left(z_G W - z_B B\right)\sin\theta + M_y \\ \left(x_G W - x_B B\right)\cos\theta \sin\phi - \left(y_G W - y_B B\right)\sin\theta + M_z \end{bmatrix} \tag{5}$$

W is the vehicle weight, *B* is the vehicle buoyancy, (both acting in the inertial z-direction) and x_B, y_B, z_B are the coordinates of the center of buoyancy in the body-fixed reference frame. ϕ and θ are the vehicle Euler angles about the inertial *x* and *y* axes, and F_x, F_y, F_z, M_x, M_y, M_z are the multiphase fluid dynamic forces and moments acting on the rigid body in the body-fixed reference frame.

FLUID FLOW MODELING

The equations of multiphase mixture fluid motion, solved in an inertial reference frame, are given in Eq 6. The formulation here is a preconditioned, dual-time, conservative form. A finite rate mass transfer model governs liquid-to-vapor and vapor-to-liquid exchange. A standard, two-equation turbulence model is applied to the mixture, and mixture viscosity is defined in a volume dependent fashion. Note that in the modeling presented here, each species is treated as an incompressible constituent. A telescoping finite volume interpolation scheme is applied. The resulting, discrete algebraic system is then identical to one based on the fundamental integral formulation of the same governing equations. Thus, as in the stationary grid presentation by Kunz [8], a *strict conservation* form results. The equations here differ from the stationary grid equations only via the grid velocity, $\xi_{j,t}$, terms, and, following the procedure in that reference, a similar, well-behaved eigensystem results.

$$\frac{\partial \hat{Q}_c}{\partial t} + \Gamma^p \frac{\partial \hat{Q}}{\partial \tau} + \frac{\partial \hat{E}_j}{\partial \xi_j} - \frac{\partial \hat{E}_j^v}{\partial \xi_j} = \hat{H} \tag{6}$$

The individual terms in Eq. 6 are defined as follows:

$$\hat{Q} = JQ = J\begin{bmatrix} p \\ u \\ v \\ w \\ \alpha_L \\ \alpha_{ng} \end{bmatrix} \quad \hat{Q}_c = JQ_c = J\begin{bmatrix} 0 \\ \rho_m u \\ \rho_m v \\ \rho_m w \\ \alpha_L \\ \alpha_{ng} \end{bmatrix} \cdots$$

$$\hat{E}_j = J\begin{bmatrix} U_j - \xi_{j_t} \\ \rho_m u U_j + \xi_{j,x} p \\ \rho_m v U_j + \xi_{j,y} p \\ \rho_m w U_j + \xi_{j,z} p \\ \alpha_L U_j \\ \alpha_{ng} U_j \end{bmatrix}$$

$$\hat{E}_j^v = J\begin{bmatrix} 0 \\ \mu_{m,t}\left[\left(\xi_{j,k}\xi_{j,k}\right)\dfrac{\partial u}{\partial \xi_j} + \xi_{j,k}\dfrac{\partial u_k}{\partial \xi}\xi_{,k}\right] \\ \mu_{m,t}\left[\left(\xi_{j,k}\xi_{j,k}\right)\dfrac{\partial v}{\partial \xi_j} + \xi_{j,k}\dfrac{\partial u_k}{\partial \eta}\eta_{,k}\right] \\ \mu_{m,t}\left[\left(\xi_{j,k}\xi_{j,k}\right)\dfrac{\partial w}{\partial \xi_j} + \xi_{j,k}\dfrac{\partial u_k}{\partial \zeta}\zeta_{,k}\right] \\ 0 \\ 0 \end{bmatrix}$$

$$\hat{H} = J\begin{bmatrix} \left(\dot{m}^+ + \dot{m}^-\right)\left(\dfrac{1}{\rho_L} - \dfrac{1}{\rho_v}\right) \\ (\rho_L - \rho_m)g_x \\ (\rho_L - \rho_m)g_y \\ (\rho_L - \rho_m)g_z \\ \left(\dot{m}^+ + \dot{m}^-\right)\left(\dfrac{1}{\rho_L}\right) \\ 0 \end{bmatrix}$$

$$J = x_\xi(y_\eta z_\zeta - z_\eta y_\zeta) - y_\xi(x_\eta z_\zeta - z_\eta x_\zeta) + z_\xi(x_\eta y_\zeta - y_\eta x_\zeta)$$

$$U_j = \xi_{j,t} + \xi_{j,x}u + \xi_{j,y}v + \xi_{j,y}w \tag{7}$$

In the flow equations solved, Eq. 6, the inviscid flux Jacobian $\partial\hat{E}_j/\partial\hat{Q}$ is similar in appearance to the stationary grid form. The only difference being the definition of U_j in Eq. 7; the grid velocity term, $\xi_{j,t}$, is now included in this definition. The partial derivatives with respect to Q of U_j are unaltered from the stationary grid system. Therefore, the algebraic mechanics to obtain the inviscid eigensystem are also unaltered. The chosen preconditioning matrix is identical to the stationary grid form and is given in Eq. 8.

$$\Gamma^p = \begin{bmatrix} \left(\frac{1}{\rho_m\beta^2}\right) & 0 & 0 & 0 & 0 & 0 \\ 0 & \rho_m & 0 & 0 & u\Delta\rho_1 & u\Delta\rho_2 \\ 0 & 0 & \rho_m & 0 & v\Delta\rho_1 & v\Delta\rho_2 \\ 0 & 0 & 0 & \rho_m & w\Delta\rho_1 & w\Delta\rho_2 \\ \left(\frac{\alpha_L}{\rho_m\beta^2}\right) & 0 & 0 & 0 & 1 & 0 \\ \left(\frac{\alpha_{ng}}{\rho_m\beta^2}\right) & 0 & 0 & 0 & 0 & 1 \end{bmatrix} \tag{8}$$

The resulting, preconditioned inviscid eigenvalues, given in Eq. 9, are identical in appearance to the stationary-grid system, again differing only in the definition of U_j. Clearly chosing β equal to a constant approximately equal to the free stream velocity results in a well-conditioned eigensystem. For work presented here, β was set equal to ten times the free stream value, this is similar to the value found (through numerical experiments) to be optimal in the stationary grid system.

$$\Lambda_j = (U_j, U_j, U_j + C_j, U_j - C_j, U_j, U_j)$$
$$C_j = \sqrt{U_j^2 + \beta^2(\xi_{j,i}\xi_{j,i})} \tag{9}$$

The mass transfer terms are defined in Eq. 10. This form has been discussed previously [8]. Based on this previous work, the value of C_ϕ was chosen (C_ϕ=100). The mixture eddy viscosity was obtained based on a wall-function-based k-ε transport model given in Eq. 11.

$$\dot{m}^- = \frac{C_\phi\rho_L\alpha_L MIN[0, p - p_v]}{\frac{1}{2}\rho_L U_\infty^2 t_\infty}$$
$$\dot{m}^+ = \frac{C_\phi\rho_v(\alpha_L + \alpha_{ng})^2\alpha_v}{\frac{1}{2}t_\infty} \tag{10}$$

$$\frac{\partial(\rho_m k)}{\partial t} + \frac{\partial(\rho_m k u_j)}{\partial x_j} = \frac{\partial}{\partial x_j}\left(\frac{\mu_{m,t}}{\mathrm{Pr}_{tk}}\frac{\partial k}{\partial x_j}\right) + P - \rho_m\varepsilon$$
$$\frac{\partial(\rho_m\varepsilon)}{\partial t} + \frac{\partial(\rho_m\varepsilon u_j)}{\partial x_j} = \frac{\partial}{\partial x_j}\left(\frac{\mu_{m,t}}{\mathrm{Pr}_{t\varepsilon}}\frac{\partial\varepsilon}{\partial x_j}\right) + [C_1 P - C_2\rho_m\varepsilon]\left(\frac{\varepsilon}{k}\right) \tag{11}$$

NUMERICAL INTEGRATION

The described model flow and rigid body motion equations are solved in the UNCLE-M code. The 6DOF model is a set of six ordinary differential equations in time and is integrated with a five-stage, fourth-order Runge-Kutta method. The same integration method was used by Dreyer et al. [6]. The flow solver is structured, multiblock, implicit and parallel with upwind flux-difference splitting for the spatial discretization and Gauss-Seidel relaxation for the inversion of the implicit operator. Primitive variable (MUSCL) interpolation with limiting based on the solution volume fraction is applied to retain higher order accuracy in flow fields containing physical discontinuities. In keeping with previous work [8], only those source terms associated with vapor production are linearized for inclusion in the implicit linear system left-hand-side. Terms associated with liquid production are treated explicitly and under-relaxed with a factor of 0.1. At each pseudo-time step, the turbulence transport equations are solved subsequent to solution of the mean flow equations. During this investigation, attention was given to temporal and spatial discretization dependence. As a requirement, to accommodate the use of wall functions, for regions of attached liquid flow, fine-grid near-wall points were established at locations yielding dimensionless wall spacing of $50<y^+<500$. In regions of separated flow, it is unlikely that this requirement was met. Based on previous experience with eddy viscosity models [8 and 9] and the apparent reasonableness of results presented here, the lack of conformity in separated regions is considered acceptable. Further details regarding the numerical method are available in Ref. [8].

COMPUTATIONAL RESULTS

A three-field (liquid, vapor, noncondensable gas) computation of turbulent mixture flow, fully coupled, via 6DOF modeling, to a supercavitating vehicle was executed. This 1.2 million node, 48 processor computation, executed on a Cray T3E system, was facilitated by a generous grant of *Challenge* computing resources from the US Department of Defense High Performance Computing Modernization Program (HPCMP).

The modeled vehicle is shown in Figure 1. Fig. 1(a) contains a schematic drawing and the basis for the notional CFD model. Fig. 1(b) shows a close-up of the cavitator and ventilation port area. This is from a steady-state computation of flow around the vehicle and illustrates the properly resolved behavior of flow around the cavitator region. The flow separates and natural cavitation is initiated at the corner of the flat cavitator. This cavitation is sufficient to envelope the gas deflectors which aid in the direction of recirculatory ventilation gas exhausting from three axisymmetric ports. The ventilation gas thus enhances and stabilizes the cavity. Due to, among several other factors, this recirculatory feature, it is supposed

that a very low rate of ventilation flow should be sufficient to support a rather large cavity. Thus it is important that this effect be captured by the flow model.

Fig. 1(c) shows the grid topology around the ventilation region. As seen in 1(b), some extent of notional vent flowpaths are modeled within the external surface of the vehicle. This is done to capture some of the shearing effect and shape the exiting vent flow profile. In Fig. 1(d) a snapshot from the computed 6DOF solution is used to illustrate the grid topology on the complete vehicle. In this case, the cavity size and shape is illustrated with an isosurface at a liquid volume fraction, α_L=0.5. Also in Fig. 1(d), the exiting propulsion plume is illustrated with an isosurface (red) of velocity magnitude. The propulsion flow is further illustrated in Fig 1(e). Here solution flow vectors are shown on the computational plane containing the blast nozzle exit flow. It should be noted that this is an incompressible solution and the interior of the propulsion nozzle was not modeled. However, it is suggested that for choked nozzle flow, the exit plane velocity, and mass flow, should be relatively constant. These velocity vectors serve to illustrate the unusual situation found when solving 6DOF problems with the flow solver in an inertial reference frame. The farfield flow velocity is zero (unless there is a "drift" value). The velocity vectors illustrate the nozzle exit velocity, directed downstream at approximately 5 times the vehicle speed, and the cavity flow adjacent to the blast tube. The cavity flow in this plane is oriented in the direction of vehicle motion, as is expected. It is part of a separated, wall bounded flow. The shape of the profile shows the flow velocity diminishing to a very small value well inside of the interface between liquid and gas, i.e. the cavity wall.

Snapshots of computed flow field are shown in Figure 2 Time histories of vehicle position and velocity are shown in Figure 3. For this computation, the Reynolds Number based on the length of the body, Re_L, is 2.3×10^8, and the Froude Number (based on vehicle length) is 13.2. The saturation vapor pressure, p_v, used in the source term for liquid vapor mass-transfer, Eq 10, is determined based on the cavitation index, σ, which is equal to 0.02. The cavity ventilation rate, C_q is 4.4. The vehicle specific gravity, γ_g is 1.3 with a uniform density. The vehicle inertial properties were estimated by subdividing the geometry into conical and cylindrical sections similar to the description by Dzielski and Kurdila [3].

In Figure 2, for the dynamic motion, the vehicle is evident within the supercavity. and appears to exhibit a limit cycle behavior. This is expected for a vehicle with no control surfaces or method of active stabilization. In the snapshots showing the dynamic behavior of the vehicle, the cavity surface is illustrated with an isosurface of liquid volume fraction equal to 0.5, and the surface of the vehicle is colored by pressure. These snapshots (from dimensionless time 1.2 to 1.55) show a cycle encompassing a complete oscillatory period. This is clear when the snapshots are compared with the zoomed-in vehicle ahead velocity plot shown in the lower portion of Figure 3. Here a peak is shown at 1.2 and again at 1.55. It is at these peaks that the high amplitude restoring force due to impact with the cavity wall occurs. Note the vehicle *skips* off of the lower cavity surface periodically, and the impact with the liquid induces a high pressure on the impact region. This impact reduces the ahead velocity and drives the vehicle upward slightly. The upward motion, concurrent with the reduction in forward velocity, can be seen in the plot of absolute vertical position. This sequence explains the remarkable inherent stability of the propelled, supercavitating vehicle as configured here and is referred to as planing mode behavior [2].

This case represents a design that is not optimized. It is likely that this case is *overventilated* such that the oscillations of the vehicle are larger than desirable. However, the vehicle still moves steadily forward, as seen in Figure 3. This is not quite obvious from the vehicle relative velocity plot, but is clear from the vehicle absolute position plot. Also, due to gravity, the vehicle initially descends slowly. Later, as the attitude of the vehicle changes, the flight path tends upwards. This again is clear from Figure 3.

In Figure 4, dynamic characterization of the long term behavior of the 6DOF UNCLE-M model of the supercavitating vehicle is illustrated. The phase plot of vertical velocity, w_B, and ahead velocity, u_B, is shown versus time. Although a simple periodic behavior is not expected from a dynamic model that has millions of degrees of freedom, it is evident that, based on the nearly repeating closed loop pattern, a quasi-periodic, developed limit-cycle is in place. This is apparent at around 3.5 time units onward, and is denoted in the figure. It is expected that more refined blowing and propulsion flow rates should result in a condition with much smaller amplitude limit-cycle oscillations. The addition of control surfaces, such as cavity piercing fins, should also reduce oscillations and, possibly, reduce the vertical drift of the vehicle [2].

Over the final four successive limit cycle periods presented here, the average ahead velocity was nearly constant and the duration of the oscillatory period remained similarly unchanged; computations were judged sufficient to describe the fully coupled dynamics. The quasi-periodic behavior is presented here using the vehicle ahead velocity and is shown in Figure 5. In Fig. 5 (a), the unsteady vehicle ahead velocity over the final four assumed periods is plotted. The period is defined as the duration between local maxima in the vehicle ahead velocity. Thus in the figure, the mean period length (normalized by initial ahead velocity, U_0, and vehicle length, L) is 0.317 and the mean ahead velocity (normalized by U_0) is 1.44. The fractional deviation from these mean quantities for each of the last four periods is shown in Fig 5 (b). From the plot it is clear that the period duration deviates by less than two percent of the mean value over these four periods. Over the final three periods, the deviation is less than one percent. Also, the mean value of ahead velocity over each of these four periods deviates by less than one half of one percent from the overall mean. Based on these observations, the uncontrolled vehicle dynamic limit cycle was considered to have been captured.

Model integration to obtain initial conditions and continuing with unsteady dynamics to the unsteady solution represented in Figures 2-5 required approximately 20.6 days of wall-clock time distributed over 48 processors or, roughly, 990 processor days.

In the fully coupled URANS-6DOF computations, the cavitation number was 0.02. It is clear from the presented results that the model vehicle motion was subject to a significant initial perturbation. Note that the vehicle velocity was allowed to vary based on the 6DOF model solution. When the computation converged to a quasi-periodic state, the mean computed ahead velocity was approximately 1.44 times the initial value. Numerous factors could affect this large increase in ahead velocity. The majority of the ahead/axial force on the vehicle was due to the integrated quantities over solid surfaces (*drag*) and the impulse through the blast tube (*thrust*). For a typical nozzle, the mass flux contributes the majority of the thrust (i.e. in the rocket thrust equation). The remainder is due to pressure differential. The mass flux was held constant throughout these integrations and determined by the initial estimation of vehicle drag from the flow solution without 6DOF modeling, at constant velocity, U_0. In the initial orientation, the vehicle was not in contact with the cavity surface, and, no significant vertical stabilizing force was present. In addition, the *drag* force based on a steady-state condition with purely horizontal flight, should differ from that force based on an unsteady integration over a vehicle operating in a quasi-periodic, planing mode limit cycle. Thus, initial perturbations of the vehicle motion were expected.

The effects of the transition from artificially held steady, horizontal flight to apparent planing limit cycle is illustrated in Figure 6. Here the evolution of the solved cavity shape is illustrated by an isosurface of mixture fluid density at 500kg/m^3. Note that the free stream liquid is assumed to have a density of 1000kg/m^3 and each of the pure noncondensable gas and vapor states are assumed to have densities of 1.kg/m^3. In this computation, the major region of impact of the cavity on the vehicle is near the region where the main cylindrical section joins with the forward conical section. This is quite clear in Figure 2. Each impact results in severe deceleration of the vehicle and a local ballooning of the cavity. The ballooning is evident in Figure 6 and the deceleration is seen in Figs. 3 and 5 (a). The duration of high deceleration is short. However, the vehicle maintains a moderate velocity for large portion of the cycle after the rebound off the cavity surface. Finally at about three quarters of the duration of the cycle (as defined by the intervals between u_B maxima in Fig. 5 (a)), the vehicle rapidly reaccelerates until the next impact.

In an effort to understand control requirements and develop tools for control design, Kirschner, et al. [2] presented a model of supercavitating vehicle dynamics and control. Compared to the coupled URANS-6DOF, this may be considered a reduced order model. However, it is well-formulated and contains much of the discernible physics and, due its relative ease of integration, represents a suitable candidate for design of control. The equations presented by Kirschner et al. model vehicle motion with respect to a cavity boundary. The boundary location is determined as an approximate solution based on potential flow theory. While the focus of their work is modeling for control, their only result presented here is for a fixed cavitator with fixed fins and in a dynamics mode supported by planing. Thus the result, for the case of a vehicle at a cavitation number of 0.03, is chosen for its qualitative similarity to the URANS-6DOF result under consideration and is presented in Figure 7. Note that in these computations, as in the URANS-6DOF results, it is the planing, or skipping, force due to vehicle contact with the cavity boundary that maintains the forward orientation of the vehicle. The resulting dynamics are periodic, or quasi-periodic.

In the result in Figure 7, the reduced frequency (fL/U_0) of simulated vehicle oscillation appears to be approximately 0.4 and the dimensionless amplitude of each cycle appears to be about 0.007. In the fully coupled URANS to 6DOF result (Fig. 2), the reduced frequency appears to be about 3.15 and the amplitude appears to be about 0.0067. Thus, the reduced frequency exhibited by the URANS to 6DOF coupled solution appears significantly higher but of similar amplitude to the simulation of Ref [2]. These discrepancies do not necessarily indicate deficiencies in either method. The model used to generate the result shown in Figure 7 contained physics that may have lead to differences including, modeled fins, a nonzero cavitator angle, a cavity shape model, and a constant axial body velocity. Thus in addition to the expected differences due to the additional degrees of freedom implicit in the URANS flow solution, additional model degrees of freedom exist, and the input modeled conditions themselves are not identical. Nonetheless, a planing mode limit cycle of somewhat similar qualities is found in both results. With appropriate discretization, the fully coupled URANS-6DOF model may contains a higher fidelity fluid dynamics model than the potential flow model. (Results of stationary grid multiphase turbulent computations have compared favorably to experimental data [8 and 9].) However, the fully coupled URANS-6DOF model has not yet been validated nor has the current result been verified. Also, with additional complexity, it is supposed that the opportunities for accumulation of modeling error is more likely.

SUMMARY

A fully coupled multiphase URANS-6DOF dynamics model has been presented. Model solutions represent a high fidelity but computationally feasible method for resolution of high Reynolds Number multiphase flow fully coupled to supercavitating vehicle dynamics. The model was applied to a nominal supercavitating vehicle configuration of research interest, ventilated and propelled by a gas jet, but without fins or other control surfaces. This model configuration was initiated in a fully developed cavity with a forward motion close to the expected terminal velocity condition. However, the final ahead limiting velocity approached approximately 1.44 times the initial value. Although the modeled vehicle contained no fins or any articulated control surfaces, a seemingly stable straight and directed forward flight path with small vertical deviation and a

limit cycle component was predicted. This is well illustrated in Figure 8, where the position of the vehicle along with the cavity boundary at regular time intervals throughout the unsteady integration is shown. Based on the discussion of Kirschner et al. [2] and Dzielski and Kurdila [3], given the proper initial conditions, movement of an uncontrolled vehicle within a stable supercavity is expected to develop to a limit cycle with a restoring force provided by periodic vehicle planing on the lower surface of the cavity. This motion was clearly observed in the integrated results. The general agreement between reduced order models and the multiphase URANS-6DOF model with regards to modes of model vehicle behavior supports the feasibility of this modeling method. In addition, the computed results independently support the concept that the forward motion of the vehicle, even in the absence of control surfaces, in the developed supercavity is fairly stable and immune to some magnitude of finite disturbances.

ACKNOWLEDGMENTS

This work was supported by the Office of Naval Research, grant #N00014-01-1-0325, with Dr. Kam Ng as contract monitor. Funding for graduate thesis research of Jason Mulherin was provided by the Office of Naval Research, grant #N00014-01-1-1041, overseen by Dr. Pat Purtell. High performance computing resources were provided through a Challenge program award from the US Department of Defense High Performance Computing Modernization Program.

REFERENCES

1. Ashley, Steven (2001) *Warp Drive Underwater*, Scientific American, **284**(5) pp. 70-79.

2. Kirschner, I.N., Kring, D.C., Stokes, A.W., Fine, N.E., and J.S. Uhlman (2002) *Control Strategies for Supercavitating Vehicles*, Journal of Vibration and Control, **8**(2) pp. 219-242.

3. Dzielski, J. and A. Kurdila (2003), *A Benchmark Control Problem for Supercavitating Vehicles, an Initial Investigation of Solutions*, Journal of Vibration and Control, **9**(7) pp. 791-804.

4. Logvinovich, G.V. (1972), *Hydrodynamics of Free-Boundary Flows*, translated from Russian (NASA TT-F-658), U.S. Dept. of Commerce, Washington, DC.

5. May, A. (1975), *Water Entry and the Cavity-Running Behavior of Missiles*, SEAHAC TR 75-2, Naval Sea Systems Command, Arlington, VA.

6. Dreyer, J., Taylor, L., Zierke, W., and F. Davoudzadeh (1997) *A First-Principle Approach to the Numerical Prediction of the Maneuvering Characteristics of Submerged Bodies*, ASME Fluids Engineering Division Summer Meeting.

7. Taylor, L.K. (1991) Unsteady Three-Dimensional Incompressible Algorithm Based on Artificial Compressibility, Doctoral Dissertation, Mississippi State University.

8. Kunz, R.F., Boger, D.A., Stinebring, D.R., Chyczewski, T.S., Lindau, J.W., Gibeling, H.J., Venkateswaran, S., and T.R. Govindan, (2000), *A Preconditioned Navier-Stokes Method for Two-Phase Flows with Application to Cavitation Predication*, Computers and Fluids, **29**, pp. 849-875.

9. Lindau, J.W., Kunz, R.F., Boger, D.A., Stinebring, D.R., and H.J. Gibeling (2002) *High Reynolds Number, Unsteady, Multiphase CFD Modeling of Cavitating Flow*s, Journal of Fluids Engineering, Transactions of ASME, vol. **124**(3) pp. 607-616.

FIGURES

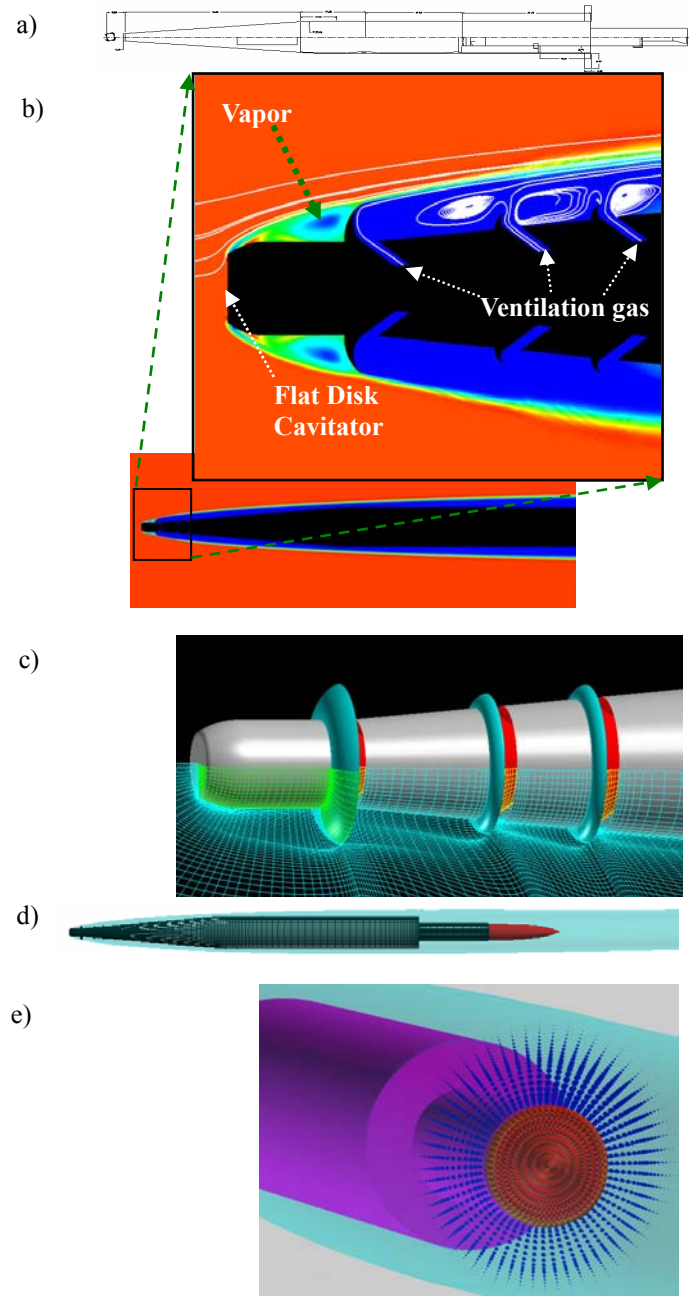

Figure 1: URANS-6DOF propelled supercavitating vehicle:
a) Schematic (basis for notional model).
b) Close-up of cavitator/ventilator illustrating recirculatory behavior.
c) Close-up of cavitator/ventilarot illustrating computational grid.
d) Snapshot from 6DOF computation showing computational grid on vehicle and propulsion plume intensity, illustrated with isosurface of velocity magnitude.
e) Close-up, snapshot from 6DOF computation showing absolute (inertial reference frame) fluid velocity vectors on the computational plane of the blast-tube exit, colored by magnitude. Cavity illustrated with isosurface of liquid volume fraction α_f=0.5.

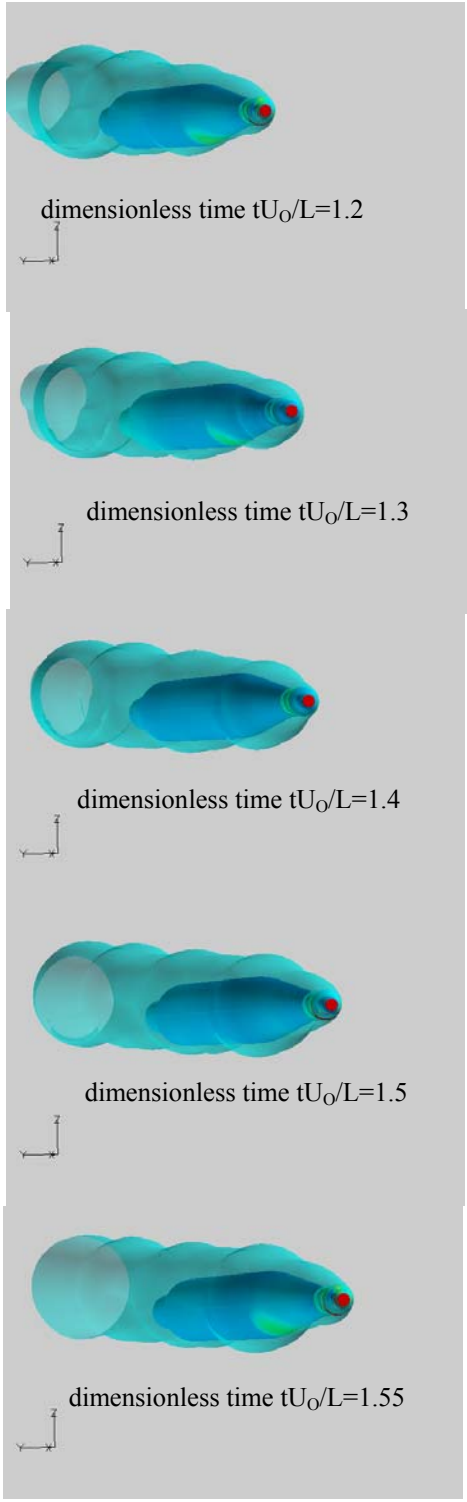

Figure 2: URANS-6DOF propelled supercavitating vehicle result: Snapshots illustrated by translucent isosurface of constant volume fraction (α_L=0.5) vehicle surface is colored by pressure level.

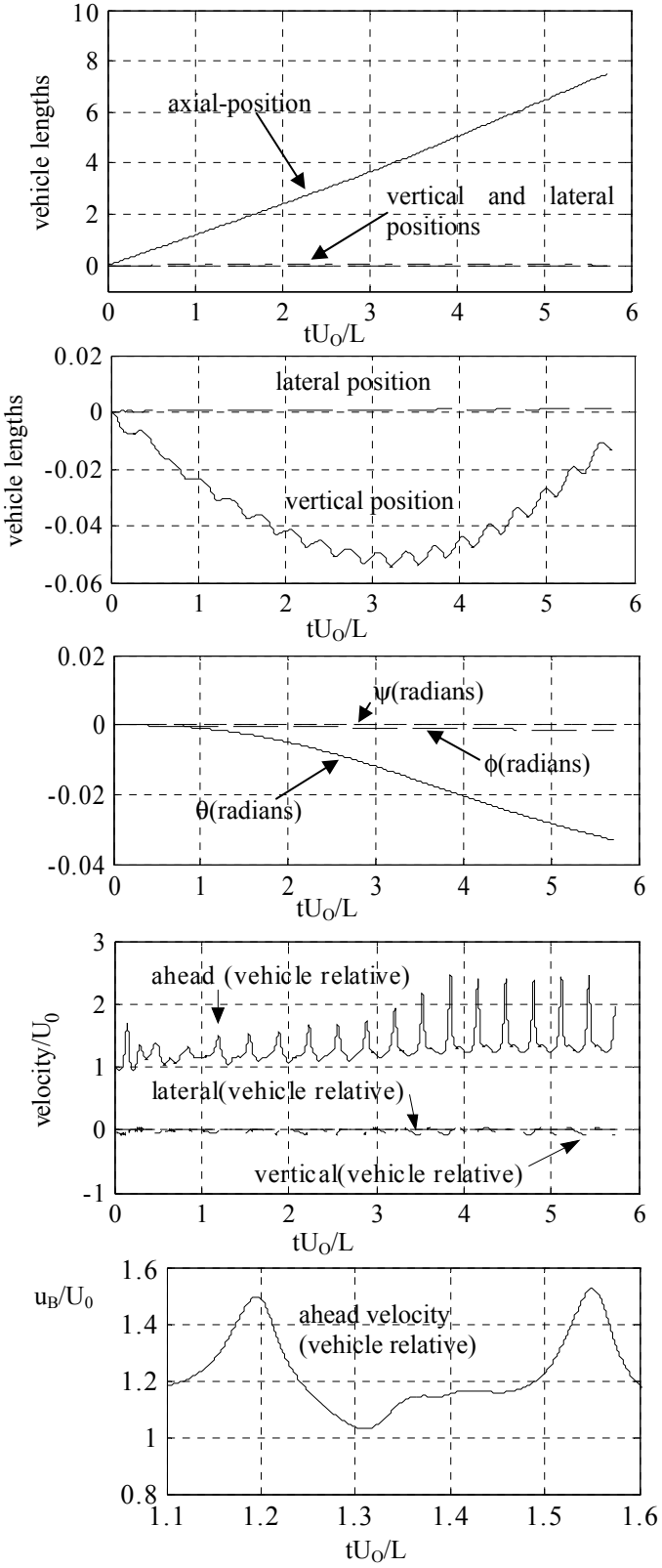

Figure 3: URANS-6DOF propelled supercavitating vehicle result: Time history plots showing absolute position and rotation and vehicle-relative velocities (u_B, v_B, w_B).

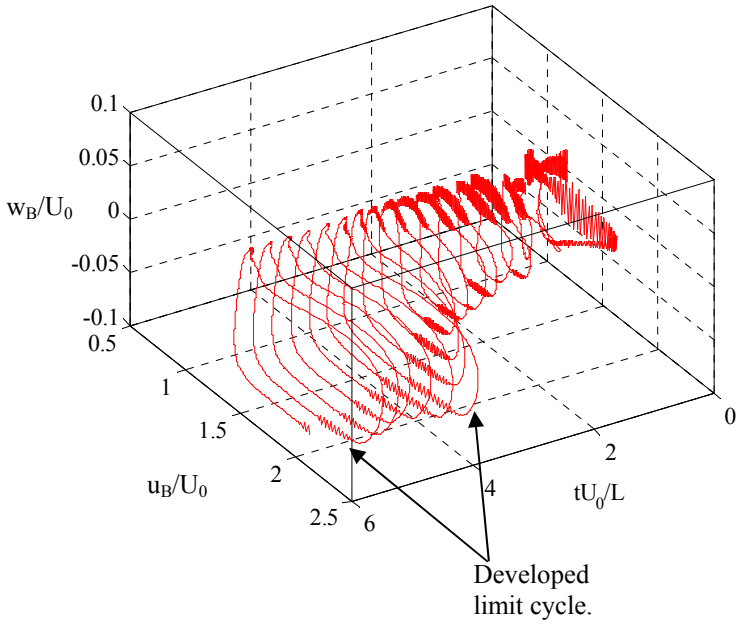

Figure 4: Limit cycle behavior:
Phase plot. URANS-6DOF propelled supercavitating vehicle result. Vehicle-relative ahead (u_B) and vertical (w_B) velocities (vehicle has no control surfaces).

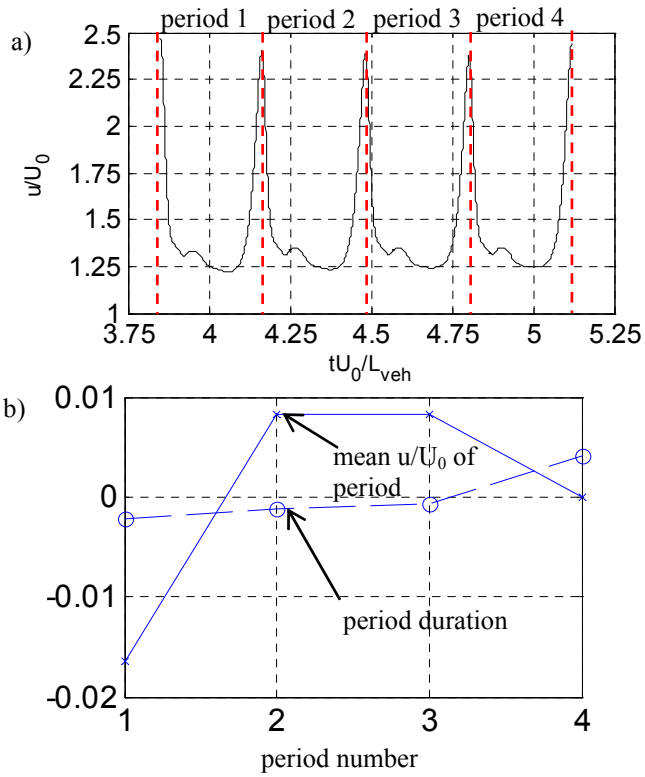

Figure 5: Convergence to quasi-periodic behavior: URANS-6DOF propelled supercavitating vehicle result over final four assumed periods, demarcated by local ahead velocity maxima.
a) Vehicle dimensionless ahead velocity versus dimensionless time.
b) Deviation of mean period quantities from mean quantities $(x_n - \bar{x})/\bar{x}$. $\bar{x}$ defined over duration of four assumed periods. Plot shows deviation of mean ahead velocity and period duration.

Figure 6: Cavity evolution from initial condition to periodic wave shape effected by planing limit cycle. Snapshots from (tU_0/L)=0 through 5.73 shown at regular intervals of duration 0.5208. Cavity illustrated by isosurface at ρ_L=500.kg/m^3.

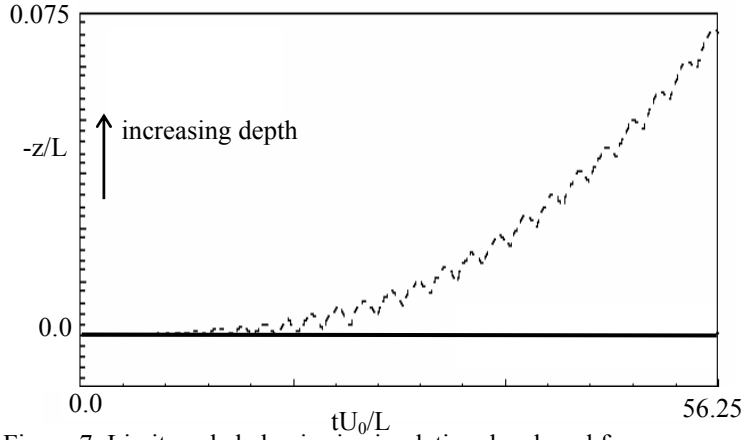

Figure 7: Limit cycle behavior in simulation developed for control [2]. Plot shows depth from initial position. Simulated, uncontrolled supercavitating vehicle (in planing mode, but with fins) at cavitation number, σ=0.03.

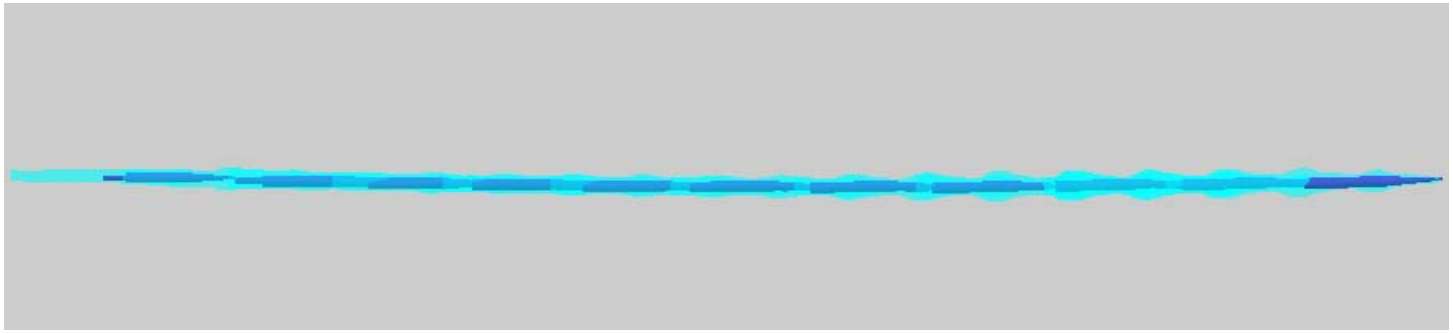

Figure 8: URANS-6DOF result. *Multiple exposure* snapshot showing vehicle position with cavity illustrated by isosurface at ρ_L=500.kg/m^3. Sequence shows solutions at dimensionless time [tU_0/L] intervals of 0.5208. Solution corresponds to time values beginning at 0.5208 and ending at 5.73 as in Figs. 2-6.